iScience

CellPress
OPEN ACCESS

Article

Active nitrogen sites on nitrogen doped carbon for highly efficient associative ammonia decomposition

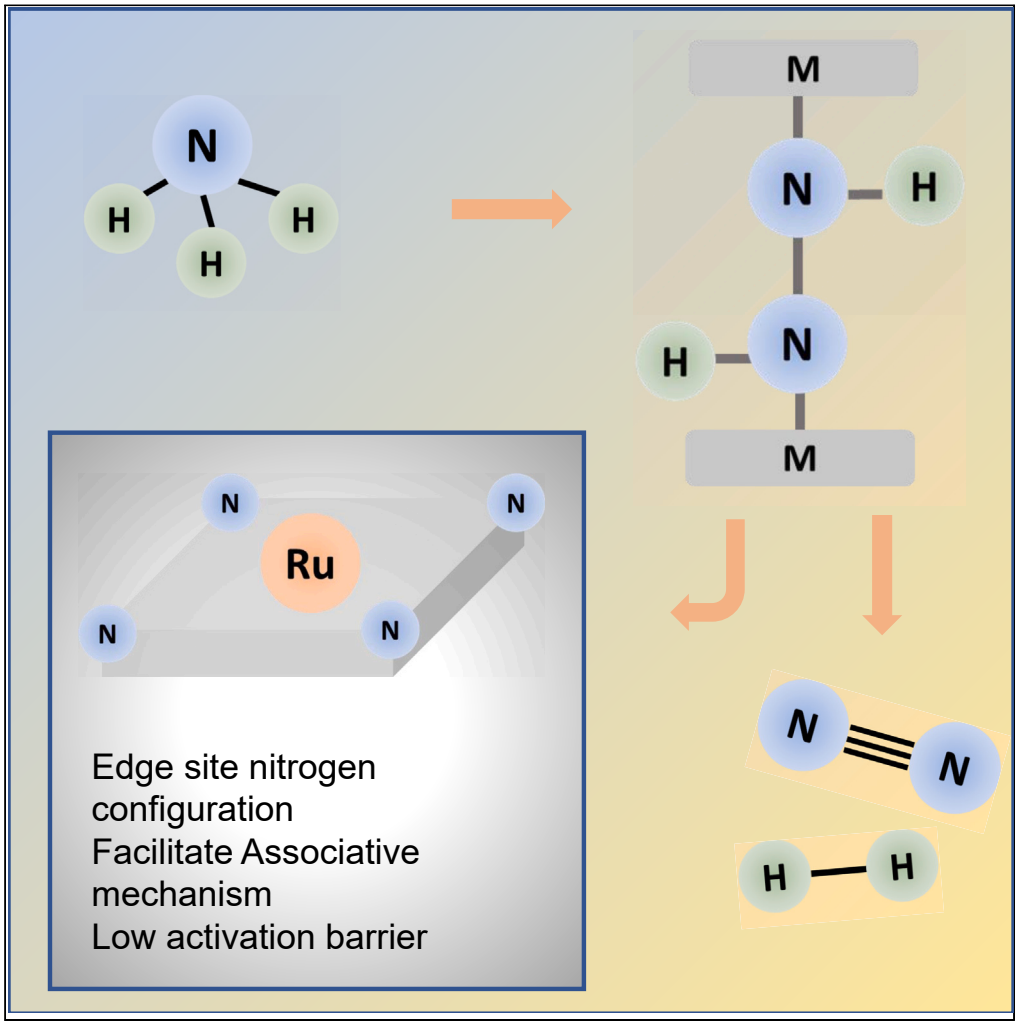

Dongpei Ye, Kwan Chee Leung, Wentian Niu, ..., Yun-Liang Soo, Simson Wu, Shik Chi Edman Tsang

edman.tsang@chem.ox.ac.uk

Highlights

Simple approach to synthesize abundant edge site nitrogen doped carbon support

High ammonia decomposition activity with low activation barrier

Associative ammonia decomposition mechanism proposed

Ye et al., iScience 27, 110571
August 16, 2024
https://doi.org/10.1016/j.isci.2024.110571

iScience

CellPress
OPEN ACCESS

Article

Active nitrogen sites on nitrogen doped carbon for highly efficient associative ammonia decomposition

Dongpei Ye,[1] Kwan Chee Leung,[1] Wentian Niu,[1] Mengqi Duan,[1] Jiasi Li,[1] Ping-Luen Ho,[1] Dorottya Szalay,[1] Tai-Sing Wu,[2] Yun-Liang Soo,[3] Simson Wu,[4] and Shik Chi Edman Tsang[1,5,*]

SUMMARY

Nitrogen doped carbon materials have been studied as catalyst support for ammonia decomposition. There are 4 different types of nitrogen environments (graphitic, pyrrolic, pyridinic and nitrogen oxide) on the amorphous support identified. In this paper, we report a 5%Ru on $MgCO_3$ pre-treated nitrogen doped carbon catalyst with high content of edge nitrogen-containing sites which displays an ammonia conversion rate of over 90% at 500°C and WHSV = 30,000 mL g_{cat}^{-1} h^{-1}. It also gives an impressive hydrogen production rate of 31.3 mmol/(min g_{cat}) with low apparent activation energy of 43 kJ mol^{-1}. Fundamental studies indicate that the distinct average Ru-N_4 coordination site on edge regions is responsible for such high catalytic activity. Ammonia is stepwise decomposed via a Ru-N(H)-N(H)-Ru intermediate. This associative mechanism circumvents the direct cleavage of energetic surface nitrogen from metal to form N_2 hence lowering the activation barrier for the decomposition over this catalyst.

INTRODUCTION

Continuous consumption of fossil fuels emits greenhouse gases which trigger severe environmental crises such as global warming, sea level rise, and extreme weathers. Consequently, studies regarding sustainable, environmentally friendly yet affordable energy vectors for future use has become an essential task. Among all potential energy suppliers, hydrogen is considered as a promising candidate. It gives not only high energy content of 120 MJ kg^{-1} by mass, but also water as the only product of combustion, which is environmentally friendly.[1]

As a non-carbon containing chemical, ammonia has been widely studied with great attention within the hydrogen economy. Owing to the high gravimetric (17.8% wt.) and volumetric (121 kg H_2 m^{-3}) hydrogen capacity, low transportation cost of liquid NH_3 at 8 bars and facilitated backward reaction for H_2 delivery with no carbon emission, ammonia is seen as an 'intermediate' green energy vector for both chemical hydrogen storage and transportation.[2] On the roadmap of using ammonia as a hydrogen carrier to power up energy plants, one essential task would be studying the process of catalytic decomposition of ammonia at mild conditions.

Traditionally, ammonia cracking over monometallic catalysts follows a dissociative process. In this mechanism, the N-H bonds of adsorbed ammonia molecules are activated on the catalytic surface to form adsorbed nitrogen and hydrogen atoms. This is then followed by surface recombination and desorption of dihydrogen and dinitrogen gaseous molecules.[3] It has been revealed by Hardacre et al. that the rate determining step involves formation of N_2 from two adsorbed nitrogen atoms (triple bonded to metal surface) at elevated temperature.[4] The activation barriers for both reversible NH_3 synthesis or decomposition is rather hard to tune due to Brønsted–Evans–Polanyi (BEP) scaling correlation.[5] This constraint states that N adsorption energy on metal surface is inversely related to N-N recombination energy. Thus, weakly adsorbed N on surface will not facilitate NH_3 adsorption but too strongly adsorption N will not favor the N-N recombination to N_2. Since the two factors cannot be varied independently, the efficiency of this catalytic pathway is limited. To break the scaling factor, an alternative associative mechanism using the Mars-van Krevelen model is introduced.[6] Under this mechanism, cleavage of weakly bound surface M-NH_x intermediate as rate determining step may be involved such that dinitrogen is formed stepwise by the dehydrogenation of the N-H bonds of two ammonia. Thus, no high energetic recombination of triple bonded nitrogen on surface from NH_3 to form N_2 is needed. The breakage of single bonded partially hydrogenated nitrogen species leads to a lower activation energy and milder reaction condition.

It is however, not yet known whether N_2 is formed between weakly bound surface NH_x from pure gaseous ammonia or somehow involving mobile nitrogen from catalyst support as in redox manner. Out of all nitrogen containing compounds, nitrogen doped carbon is considered as

[1]Wolfson Catalysis Centre, Department of Chemistry, University of Oxford, Oxford OX1 3QR, UK
[2]National Synchrotron Radiation Research Centre, Hsinchu 30076, Taiwan
[3]Department of Physics, National Tsing Hua University, Hsinchu 30013, Taiwan
[4]Oxford Green Innotech Limited, 9400 Garsington Road, Oxford Business Park, Oxford OX4 2HN, UK
[5]Lead contact
*Correspondence: edman.tsang@chem.ox.ac.uk
https://doi.org/10.1016/j.isci.2024.110571

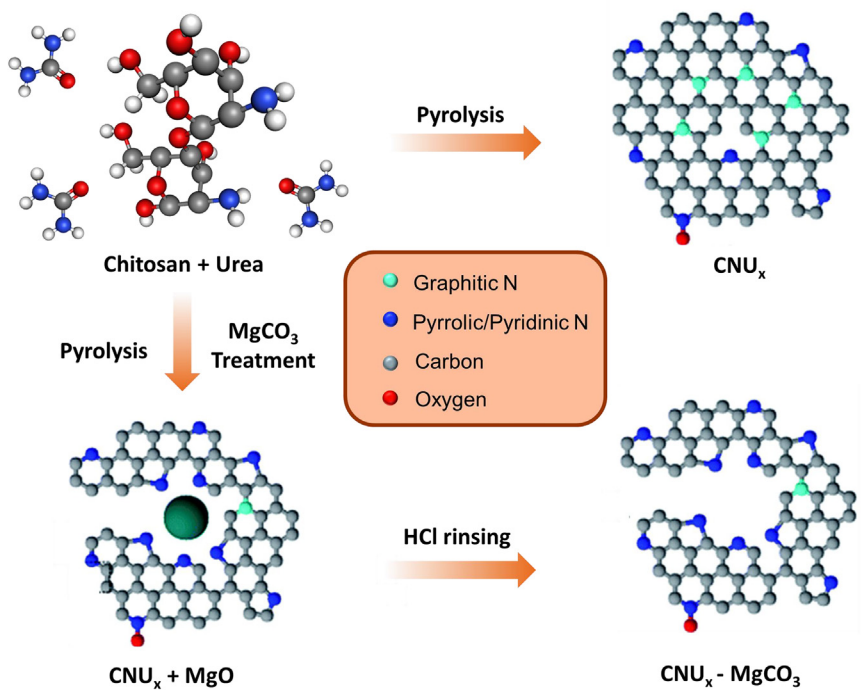

Figure 1. Schematic illustration of the synthetic process
Reproduced and modified in part from ref [11].[11]

an outstanding catalyst to facilitate metal dispersion.[7,8] Although it is widely studied, the nature of metal support interaction is still unclear including the role of different nitrogen environment (graphitic, pyrrolic and pyridinic) during the associative ammonia cracking catalysis.

Chitosan is a polymer containing β-linked D-glucosamine and N-acetyl-D-glucosamine which is extracted from the outer skeleton of crab, lobster and shrimp.[9,10] Since it is a low cost, sustainable and yet easily processable biomass, chitosan is therefore used as a carbon precursor to synthesize the nitrogen doped carbon support. In our recipe, nitrogen doped carbon support is synthesized by calcinating chitosan with urea. As urea can act as the nitrogen source and alter the nitrogen content on the catalyst support. The final product is denoted as CNU_x where x is the chitosan to urea ratio. To understand the effect of nitrogen toward the catalysis reaction, the synthetic procedure is modified by addition of $MgCO_3$ to control the formation of nitrogen configuration. $MgCO_3$ can catalyze the decomposition of carbon in air and release carbon dioxide during calcination via $MgCO_3$/MgO recycle, a schematic illustration of the synthetic process is shown on Figure 1. The residual MgO species is rinsed to obtain the final product, denoted as CNU_x-$MgCO_3$.

In this paper, a nitrogen doped carbon material support with high nitrogen content has been synthesized and presented. Our catalyst, 5% Ru CNU_3-$MgCO_3$ shows a superior catalytic performance toward ammonia decomposition with an exceptional low activation barrier of 43 kJ mol^{-1}. The strong interactions between edge site nitrogen species on the support (pyrrolic and pyridinic N) and Ru metal sites are studied using a range of characteristic techniques in order to elucidate the fundamental mechanism. This work could provide insights on future catalysts design for the heterogeneous activation of ammonia and other potential processes.

RESULT AND DISCUSSION

Material synthesis and characterization

The bulk structure of the support CNU_3 was analyzed by Fourier transform infrared spectroscopy (FTIR). As shown in Figures S1 and S2, distinct peaks observed at 2850, 2920 and 2960 cm^{-1} which are ascribed to symmetric stretching vibration of C–H bond. The remaining peaks lie within the range of 1300–1700 cm^{-1}, which are mainly accounted toward C–H bending (at 1425 and 1373 cm^{-1}) and the stretching modes of C-N heterocycles in the nitrogen doped carbon (at 1545 and 1649 cm^{-1}).[11,12] There is also a double peak at 2330 and 2360 cm^{-1} shown on the spectrum which corresponds to C-O, that may come from small residual carbon dioxide trapped from air.[13] FTIR study for CNU_3-$MgCO_3$ appears to be similar with the major peaks ascribed to the C-H and the C-N bonds. No additional peaks are found for Mg-O bond, indicating the successful removal of residual MgO and $MgCO_3$ from the N-doped carbons. This feature is also confirmed by XRD, which shows two broad peaks at around 25.8° and 44.0° accounting to the (002) and (100) planes of hexagonal graphite structures on the amorphous carbon nitrogen layers (Figure 2A).[14] Moreover, the disappearance in MgO peaks at 2θ = 36.9, 42.9, 62.3, 78.6 (which are associated at (111), (200), (220) and (222) planes) on the XRD pattern is also a strong evidence of the successful removal of residual MgO species.[15]

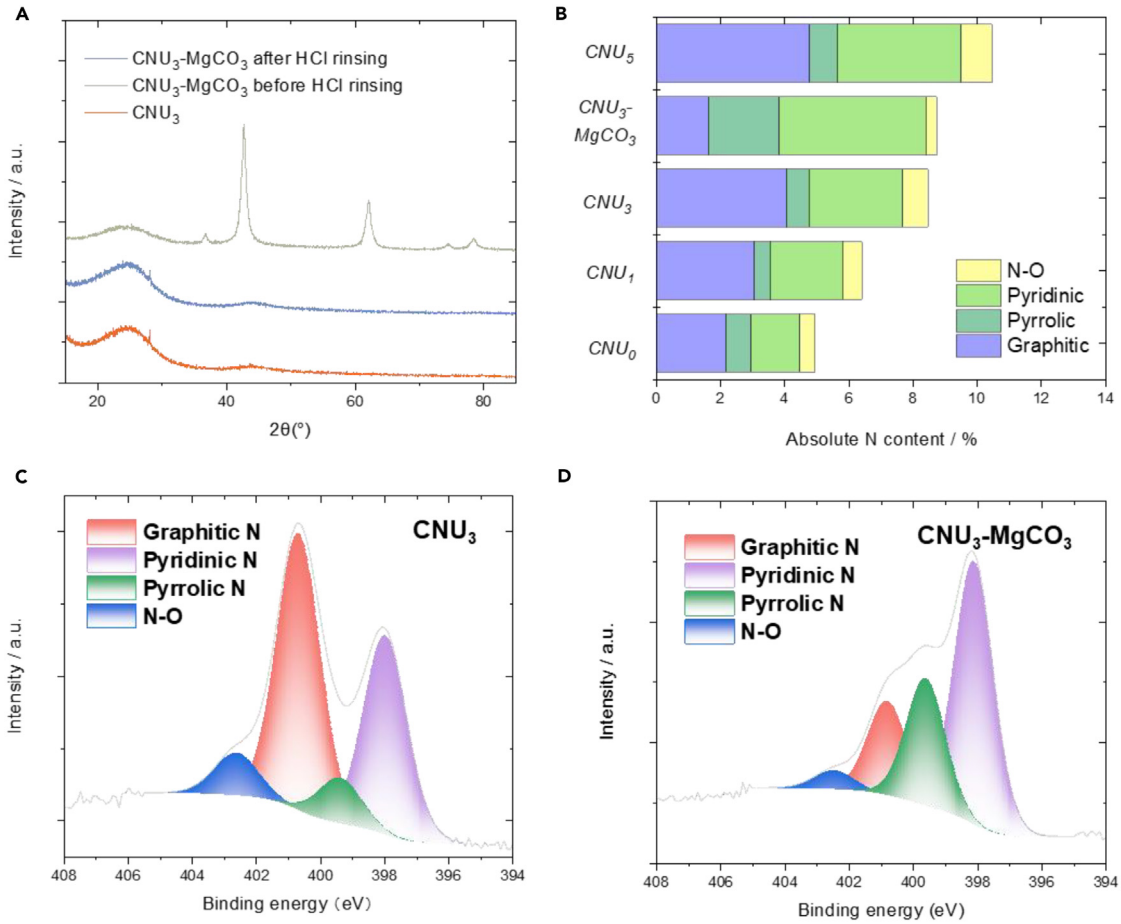

Figure 2. Structural information of the sample

(A) XRD of the analogue material (B) The atomic percentage of Nitrogen on the analogue supports calculated from XPS (C) N1s XPS spectrum of CNU_3 (D) N1s XPS spectrum of CNU_3-$MgCO_3$.

To gain insight on the types of nitrogen species in these samples, X-ray photoelectron spectroscopy (XPS) was carried out. As illustrated in Figure 2B, with increasing content of urea in our recipe during the synthesis, the N content of the final carbons indeed increases (4.95, 6.45, 8.95, and 11.95% for CNU_0, CNU_1, CNU_3 and CNU_5, respectively, Table S1). This is a clear indication of successful doping of nitrogen into the support. The surface of the support was further investigated using a high-resolution N 1s XPS spectra to understand the specific nitrogen environments. As presented in Figures 2C and 2D, the resultant spectra are deconvoluted into at least 4 different peaks located at 398.2, 399.6, 400.8 and 403.1 eV, which can be assigned to pyridinic-N, pyrrolic-N, graphitic-N (quaternary) and N-oxide (small quantity) species respectively.[16] Nitrogen on the CNU_x samples mainly exists as graphitic nitrogen with an N content of 48.04%, followed by pyridinic *N* 34.56%. This nitrogen environment of the support hardly changes with increasing content of urea as indicated by the spectra. However, a clear shift in the N environment on the catalyst support has been noted especially when the sample was treated with $MgCO_3$. The content of graphitic N dramatically decreases from 48.04% for CNU_3 to 18.72% for CNU_3-$MgCO_3$, accompanying with an increase in the pyrrolic and pyridinic N contents (from 8.21% to 25.28% and 34.56%–52.25%, respectively, Table S1). This clearly gives the correlation between graphitic nitrogen with the pyridinic/pyrrolic nitrogen: the nitrogen atoms that replaced carbon atoms in graphitic structure can be exposed as nitrogen sites in forms of pyrrolic and pyridinic nitrogen. The O content in CNU_3-$MgCO_3$ can also be further reduced during $MgCO_3$ treatment. The increasing exposed nitrogen sites appear to give higher ammonia decomposition catalysis as shown at later session. High-resolution O 1s spectra is also deconvoluted into 4 peaks, which corresponds to C=O at 531.2 eV, C–O–C at 532.6 eV, C–OH at 533.9 eV and O-N at 536.2 eV respectively (Figure S3).[17] Since the oxygen content is low and remains at a relative constant level for all tested samples, it is therefore suggested that they may not play the major role in the overall ammonia decomposition catalysis.

Brunauer–Emmett–Teller (BET) surface area analysis has been carried out to understand the pore size distribution as well as the specific surface area. A positive progressive correlation has been found between the nitrogen content and the specific surface area/porosity, showing a better exfoliation and larger porous level when more urea has been used during the synthesis (Table S2). The CNU_3 support shows a hysteresis loop with an II type isotherm from the nitrogen adsorption-desorption measurements. Interestingly, this feature changed to a IV type

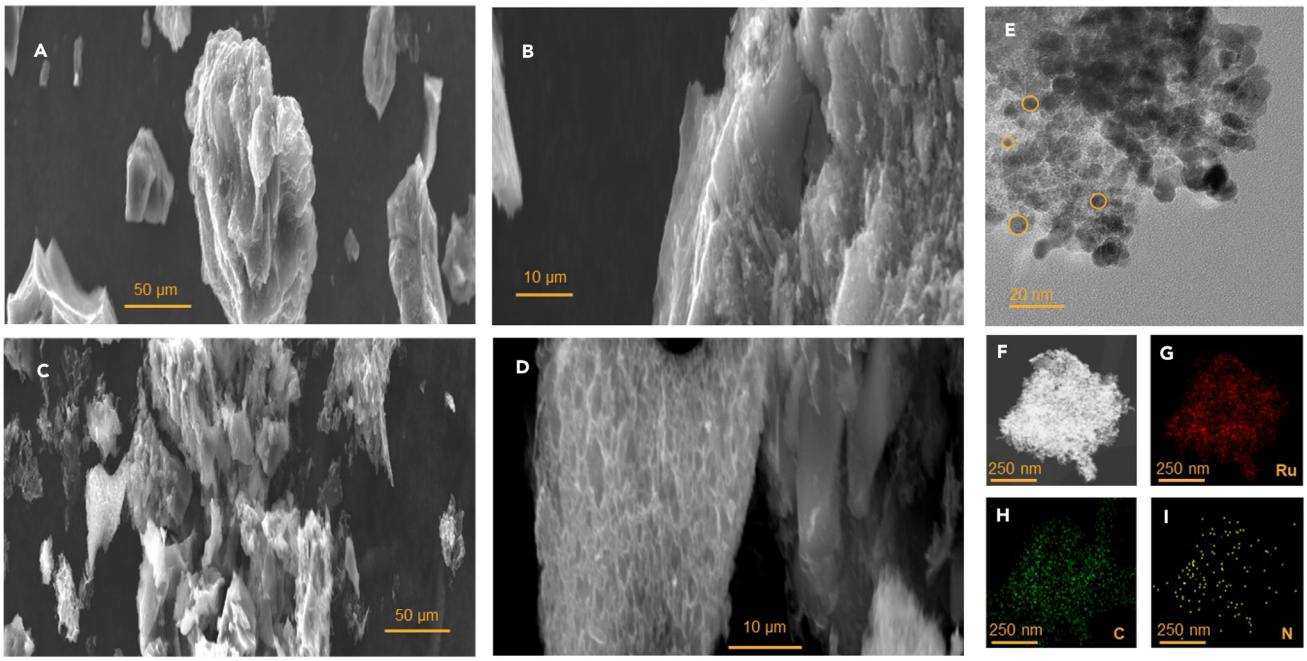

Figure 3. Morphology and microstructure of the support

SEM image under different resolution for (A and B) CNU_3 (C and D) CNU_3-$MgCO_3$; (E) TEM image (F) STEM image (G–I) elemental mappings over 5%Ru CNU_3-$MgCO_3$ catalyst.

isotherm for the CNU_3-$MgCO_3$ support, indicating the presence of distinct meso-pores (Figure S4).[18] The additional porous structures lead to spectacular increase in specific surface area from 121 m^2/g of CNU_3 to 205 m^2/g for CNU_3-$MgCO_3$ (Table S2). The change of morphology of the supports is in alignment with the results by scanning electron microscopy (SEM). As shown in Figures 3A–3D, the CNU_3 sample exhibits as a dense rigid block with a large particle size of up to 100 μm and no pores found. On the other hand, CNU_3-$MgCO_3$ shows a fluffier and sponge-like structure. The material layers are packed looser and a smaller particle size is noticed. Besides, macropores as well as mesopores on the carbon blocks for the CNU_3-$MgCO_3$ support is clearly observed. Further high-resolution transmission electron microscopy (TEM) was performed over 5 wt. % Ru impregnated CNU_3 and CNU_3-$MgCO_3$ catalysts. It is noted that Ru are well dispersed on both supports (Figures 3G and S5C). However, Ru on CNU_3 exhibits a nanoparticle (NPs) size of a range between 10 and 20 nm, which is larger than the Ru NPs size (<10 nm) of 5%Ru CNU_3-$MgCO_3$. The actual Ru loadings on the two supports are measured using inductively coupled plasma mass spectrometry (ICP-MS). An almost identical Ru loading of around 4.6 wt. % on CNU_3 and CNU_3-$MgCO_3$ support has been calculated (Table S3). The result from TEM and ICP-MS also suggest a higher surface area exhibits by the $MgCO_3$ treated support as it owes a better Ru dispersion. Moreover, both supports are amorphous and do not exhibit distinct graphitic lattice structures, as can be deduced from the non-uniform sizes of the Ru NPs (indicated by the orange circles) illustrated in Figures 3E and S5A.

The $MgCO_3$ addition during the synthetic process indeed leads to the formation of distinct meso and macro-pores. It is anticipated that a mixture of chitosan, urea would form a gel-like structure in the presence of acetic acid. Meanwhile, acetic acid would partially react with the induced $MgCO_3$ to emit carbon dioxide and hydrogen. Leaving pores within the as-synthesized product. Moreover, it has also been postulated that during the calcination, $MgCO_3$ would decompose into MgO. This reaction is accompanied with the release of carbon dioxide, which further reacts with carbon/oxygen atoms to form CO.[19] This effect enlarges the existing pores and creates new pores. From another point of view, the reaction of CO_2 with on-site carbon atom would form more exposed edge sites of the graphitic sheets. Since pyrrolic and pyridinic nitrogen are located at exposed edge sites. It explains the increase in pyrrolic and pyridinic nitrogen content at the expense of graphitic nitrogen as the formation of these two types of nitrogen are favored.

Ammonia decomposition catalysis

5%Ru on nitrogen-doped carbons were tested by placing 50 mg each in a vertical fixed-bed flow reactor. As illustrated in Figure 4A, at 500°C and WHSV = 30,000 mL g_{cat}^{-1} h^{-1}, increasing nitrogen content along with increasing surface area would have a positive effect on the catalysis as the ammonia decomposition rate significantly increases. It then reaches a peak conversion of 64.7% for 5%Ru CNU_3. A decrease in activity is then noted for 5%Ru CNU_5, giving a conversion of around 45% despite the increase in N content at even higher surface area. Similar trend is also found for different Ru loading (Figure S6). Although 10 wt. % Ru loading on the nitrogen doped carbon support illustrates a higher ammonia conversion rate compared to 5 wt. % Ru loading. The catalytic experiments were still performed under 5 wt. % metal loading as the conversion efficiency of the best 5%Ru CNU_3 catalyst is already superior/comparable to most of our conventional catalysts tested. Ru

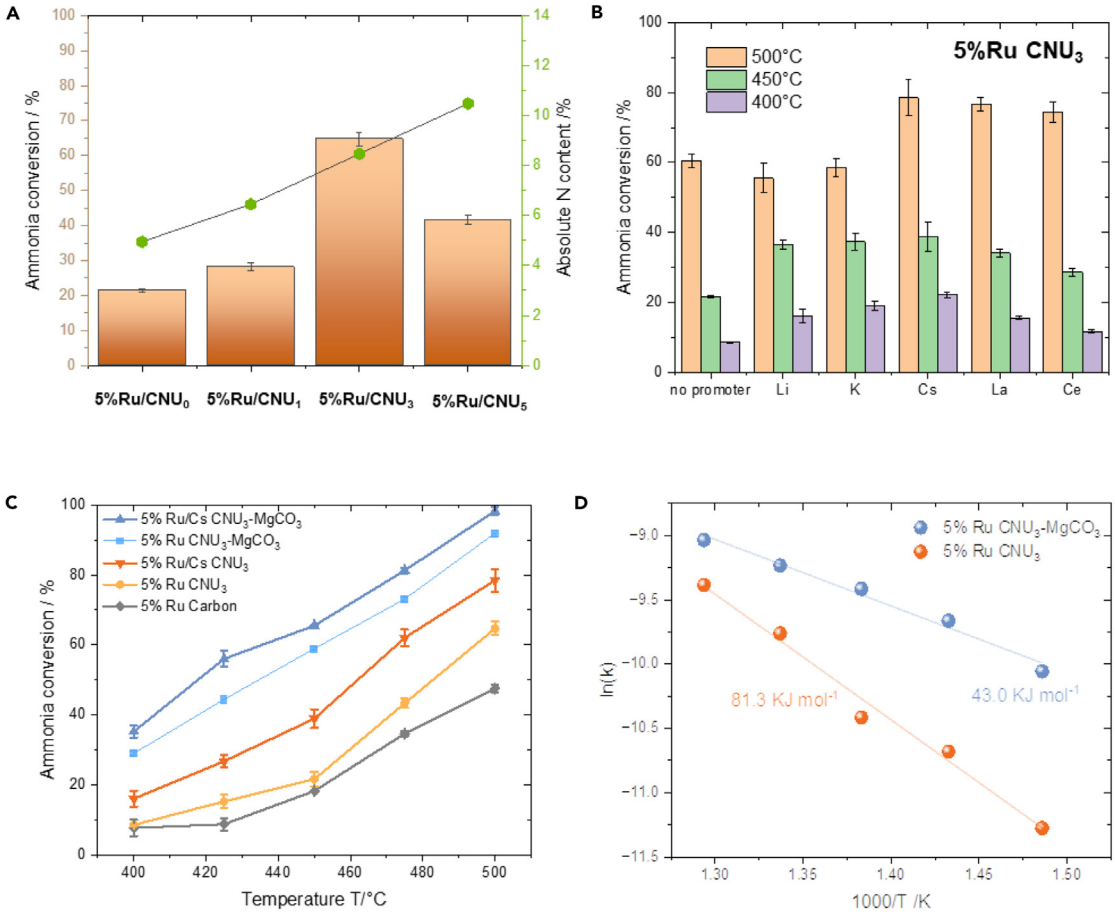

Figure 4. Catalytic performance test for ammonia decomposition at weight-hour space velocity (WHSV) = 30,000 mL g_{cat}^{-1} h^{-1}

(A) Relation between NH_3 decomposition activity and absolute N content tested at 500°C.

(B) NH_3 conversion of 5%Ru CNU_3 with different alkaline promoters. (Ru: metal promoter molar ratio is 1) (C) NH_3 decomposition reaction as a function of temperature over different Ru supports.

(D) Arrhenius plots of supported Ru samples.

is an expensive ingredient so maintaining high activity at lower metal loading is more desirable. While the ammonia conversion increases along with increasing nitrogen content as well as surface area/porosity increases, it reaches a maximum conversion rate at CNU_3. Overall, nitrogen doping exerts a positive effect on ammonia decomposition. Catalysis on nitrogen doped carbon support was carried out and little conversion toward ammonia decomposition was observed, indicating that the activity of the catalyst is mostly routed from the Ru metal (Figure S7). We attribute to the fact that as an N-doped carbon support for Ru NPs, the one electron addition of N atoms replacing C atoms in graphite structure can increase electron density availability over the delocalized p-π system of graphite sheet hence enhancing the electronic donating properties of the carbon support, adding toward the increasing basicity of the support.[20] This will easily allow electron transfer from the nitrogen doped supports to Ru NPs and increasing the activity of Ru for ammonia decomposition. However, on the other hand, the direct contact between excessive nitrogen sites with Ru particularly in CNU_5 is not desirable in catalysis, which withdraw electron density from Ru NPs locally.[21] This will weaken the adsorption of surface nitrogen species via a lesser degree of back bonding, leading to a negative impact on the ammonia decomposition reaction. It is worth noting that increasing surface area would commonly lead to a better metal dispersion, more active sites and thus a better catalytic activity. However, for the 5%Ru CNU_5 catalyst, even that it is demonstrated to be the largest surface area among others, it gives a lower conversion compared to 5%Ru CNU_3. If we normalize the activity per surface area for CNU_0 to CNU_3 (Figure S6 and Table S2) it is apparent that we can see the correlation in their ammonia decomposition rate alongside with the increase in their N content (Table S1). Thus, the increase in catalytic activity could be attributed to the synergetic effects of surface area and nitrogen content. However, the signature lower NH_3 conversion of 5% Ru CNU_5 than 5% Ru CNU_3 despite its higher surface area (Figure S6 and Table S2) also indicates that there could not be a simple correlation. Instead, the higher nitrogen content and configuration in CNU_5 may exceed a kind of critical level exerting a negative impact on the catalysis, which could play a major factor in catalysis. Thus, these antiparallel effects clearly contribute to the 'volcano' shaped activity, as shown on Figure 4A.

Table 1. Catalytic performance of Ru on nitrogen doped carbon material compared with the literature data for NH_3 decomposition

Catalysts	Ru (wt %)	T(°C)	WHSV (NH_3 mL g_{cat}^{-1} h^{-1})	Conv. (%)	E_a/kJ/mol	Reference
Ru CNTs	5	500	60000	ca. 43	71.4	Yin et al.[32]
Ru N-carbon	5	450	6000	ca. 80	ND	Ren et al.[33]
Ru N-CNTs	7	400	6000	48.0	85.3	Bell et al.[34]
Ru ZrO_2	3	550	30000	ca.20	117	Zhang et al.[35]
Ru Al_2O_3	4.8	500	30000	17.6	61.2	Kim et al.[36]
Ru MgO	5	500	30000	42.8	102.7	Ju et al.[37]
Ru Cr_2O_3	5	500	30000	ca. 25	75.8	Li et al.[38]
Ru CNU_3	5	500	30000	64.7	81.3	This work
Ru/Cs CNU_3	5	500	30000	79.8	63.8	This work
Ru CNU_3-$MgCO_3$ treated	5	500	30000	91.2	43.0	This work
Ru/Cs CNU_3-$MgCO_3$ treated	5	500	30000	99.7	38.8	This work

WHSV, weight-hour space velocity ;E_a, activation energy.

Various further promoters were impregnated on 5%Ru CNU_3 sample with a Ru/metal promoter molar ratio of 1 to study the effect of promoters toward the ammonia decomposition catalysis. As shown in Figure 4B, the general order of catalytic activity ≤450°C follows the order Ru/Cs CNU_3 > Ru/K CNU_3 > Ru/Li CNU_3 > Ru/La CNU_3 > Ru/Ce CNU_3, reflecting the beneficial effect of increasing electron donating ability of these promotors, as discussed. However, it is interesting to note that an unexpected activity boost of the catalysts at highest temperature (500°C), particularly with lanthanum and cerium samples, giving a very different activity order. The precise reason for this activity boost is not yet clear, which may have to be investigated in detail. However, this may relate to additional properties of lanthanides which are known to assist hydrogen migration for ammonia decomposition reaction at elevated temperature.[22–24] Nonetheless, Ru/Cs CNU_3 sample shows the best activity throughout the temperature range. Effect of promoters for NH_3 decomposition, especially for Ru-based catalyst systems have been reported in literature. It has been suggested that incorporation of alkali metal hydroxide (e.g., KOH) can decrease the nitrogen desorption temperature and hence increases the dissociation rate.[25] Furthermore, it is well recognized that electronic promoters can increase the electron density of the active Ru site.[26–28] Thus, the combination of Cs with N incorporation to graphitic structure can clearly offer the best electron donation to Ru from the promoted support.

To further explore the effect of different nitrogen configurations toward the catalysis, CNU_3-$MgCO_3$ was particularly synthesized and compared with CNU_3 and pure carbon sample support. The results are illustrated in Figure 4C. As shown, the nitrogen doped support, 5%Ru CNU_3 shows a higher conversion rate compared to the commercial 5%Ru on carbon material. This is in agreement with our previous discussion on the beneficial effect of N atoms substitution to C atoms in graphitic support which can enhance the overall reaction activity. However, more interestingly, we note the $MgCO_3$ treatment can introduce unusual behavior. There is a noticeable dramatic increase of conversion from 64.7% to 91.2% at 500°C for 5%Ru CNU_3 and 5%Ru CNU_3-$MgCO_3$, respectively. Even at lower temperature, the 5%Ru CNU_3-$MgCO_3$ shows a more superior conversion of 59% and 20% at 450°C and 400°C, respectively. The activity of 5% Ru CNU_3-$MgCO_3$ shows ~90% NH_3 conversion while 5% Ru CNU_5 shows only ~40% NH_3 conversion under the same conditions (see Figures S6 and S7). Notice that their surface area of CNU5 of 217.50 m^2g^{-1} is slightly higher/comparable to CNU_3-$MgCO_3$ of 205.64 m^2g^{-1} (Table S2). Thus, it appears that the nitrogen content and configuration again (Table S1) would play a more important role than that of the surface area in the activity determination. Kinetic studies on the two samples 5%Ru CNU_3 and 5%Ru CNU_3-$MgCO_3$ have been further performed to find out their apparent activation energies. By using the Arrhenius equation, a linear fitting of Ln (reaction rate) with inverse temperature at low conversion values has been obtained. As can be seen from Figure 4D, the apparent activation energy E_a of the nitrogen doped carbon catalyst has been decreased from typical 81 $kJmol^{-1}$ for 5%Ru CNU_3 to 43 $kJmol^{-1}$ for the $MgCO_3$ treated sample. With addition of Cs promoters, the 5%Ru/Cs CNU_3-$MgCO_3$ sample can reach an ammonia conversion of 99.7% and a hydrogen production rate of 31.3 mmol/(min g_{cat}). As seen from the Table 1, the specific activity of our $MgCO_3$ modified nitrogen doped carbon sample out-performs most of the state-of-the-art catalysts such as Ru/carbon nanofiber (Ru/CNFs), Ru/carbon nanotubes (Ru/CNTs) and Ru/MgO with the typical apparent activation energies of 70–110 $kJmol^{-1}$.[29–31] Notably, 5%Ru CNU_3-$MgCO_3$ was continuously tested in a flow reactor for a 24 h period. Figure S8 shows no significant drop in NH_3 decomposition conversion. This indicates that the Ru active sites and its nitrogen doped carbon support are stable throughout the catalysis. The structural feature is further analyzed by XPS which is discussed later in this paper.

Further characterization and mechanism understanding

It is well accepted that the kinetic barrier of Ru NPs on various supports for ammonia decomposition reactions would have such high values due to dissociative mechanism. However, 5%Ru CNU_3 sample exhibits a lower activation energy. This feature may indicate other concurrent mechanism such as associative mechanism over some dispersed Ru species rather than Ru particles. Interestingly, the apparent E_a value of 5% Ru CNU_3-$MgCO_3$ is attenuated to 43 kJ/mol when $MgCO_3$ treatment was introduced. It highlights the importance of different Ru species and corresponding mechanisms toward the overall catalysis.

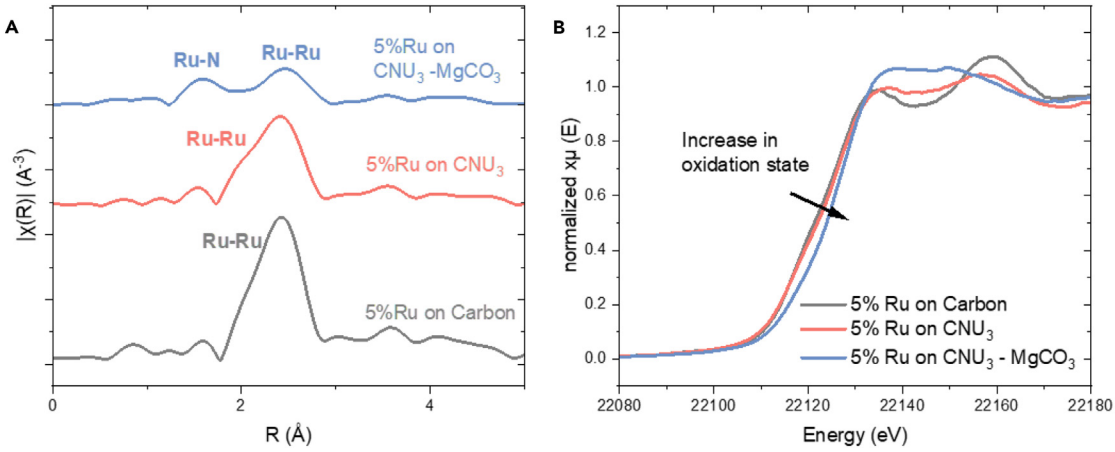

Figure 5. XAS result over Ru K-edge

Ru K-edge XAS results for the Ru loaded samples (A) Fourier transform of the EXAFS signals (B) XANES spectra.

Noticeably, 5%Ru CNU_3-$MgCO_3$ sample gives almost 1.5 times larger ammonia conversion rate than 5%Ru CNU_3 catalyst despite the fact that XPS measurement indicated a similar absolute nitrogen content of ca. 8.5% for both supports. As discussed, the content of the edge site nitrogen (pyrrolic and pyridinic nitrogen) has significantly increased from 43% to almost 80% at the expense of graphitic nitrogen due to the fragmentation of graphite to mesoporous partial graphitic structure upon the $MgCO_3$ treatment. This structural change in morphology and chemical configuration leads to exposed and more accessible nitrogen sites which was reflected by X-ray absorption spectroscopy (XAS). Figure 5 illustrates the results for XAS at the Ru-K edge of the samples. As shown, for 5%Ru on carbon and 5%Ru CNU_3, one main peak at 2.67 Å is recorded which can be assigned to the typical metallic Ru-Ru in Ru NPs. The average coordination number of Ru drops from 10 to 8 and 6, respectively due to smaller particle sizes, which is in alignment with the observation from TEM result (Table S4). We do not expect the added Ru can be too well dispersed since conjugated graphitic sheet structure do not facilitate complexation to Ru ions hence the major Ru species would be in form of Ru NPs after the synthesis as reflected by the XAS and TEM. The incorporation of N to carbon support thus stabilizes Ru NPs, the electron donation of N-doped carbon to Ru NPs is therefore anticipated as the main way to facilitate the breakage of N-H bonds via dissociative mechanism.[39] However, the introduction of $MgCO_3$ toward the synthesis breaks down the graphitic nitrogen arrangement of the carbon material and forms 'holes' with easily accessible edge site nitrogen which can chelate Ru species. This is in agreement with the arisen of a new distinct Ru-N peak as shown at 2.04 Å (stabilized Ru ions) at the expense of Ru-Ru peak (decrease quantity of Ru NPs). Furthermore, the significant positive shift in X-rays absorption K edge for Ru indicates the increase in oxidation state as shown in Figure 5B. This confirms the existence of significant quantity of discrete Ru ions (ca. Ru^{3+}) along with Ru NPs (Ru-Ru). The average coordination for Ru-N within experimental error for this region is determined to be 4.03 ± 0.48 in the meso-/macro pores. This is in alignment with the increase in catalytic activity since the quantity of N-containing edge sites are more accessible and have a stronger metal-support interaction. It is well recognized that in Ru based catalysts, the Ru atom arrangement in B5 structure provides the active site for the ammonia synthesis and decomposition reaction. Nonetheless, for such catalysts, the reaction follows a dissociative mechanism and exhibiting slower rate with an activation energy of 70–110 kJ mol^{-1}. This is definitely not the case for 5%Ru CNU_3-$MgCO_3$ as it shows a much higher activity with lower activation energy indicative of the associative mechanism. Thus, it is suggested that the significant raise in activity of the $MgCO_3$ treated sample is mainly attributed toward the formation of discrete Ru specie anchored by 4 nitrogen configurations.

Temperature programmed reduction (H_2 TPR) was used to reflect the differences in Ru species between 5%Ru on carbon, 5%Ru CNU_3 and 5%Ru CNU_3-$MgCO_3$. As seen in Figure 6A, there are two peaks observed: one peak in the range of 50°C–200°C and the other broad peak appearing after 450°C. The first peak corresponds to the reduction of oxidized Ru species while the later one is attributed toward the catalytic methanation and gasification of carbon by H_2 over Ru.[40,41] As seen from the enlarged figure of first peak region (Figure 6B), there is a remarkable peak shift and peak size enhancement in the first reduction peak of the Ru species from 90°C to 105°C when N is doped on the support. An even larger peak shift and enhancement in peak size increase are also observed when the support is treated with $MgCO_3$. These observations agree with the XAS result as an indication of the increasing stronger stabilization of oxidized Ru ions with surface nitrogen than graphite or N-doped graphite samples. The exposed pyrrolic and pyridinic nitrogen sites offer a stronger interaction accounting for the higher degree of temperature shift. Edge site nitrogen located in structural less rigid sheets in mesopores offers chelation to metal ions Ru^{3+} adsorbed on the surface of support than that of the graphitic nitrogen. The unbonded electron pair from the nitrogen species would thereby be able to bind with Ru^{3+} as a ligand and anchor the metal species. The result highlights the importance of surface nitrogen configuration and indicates the promising role of edge exposed nitrogen sites toward the ammonia decomposition catalysis.

In situ FTIR was employed on the 5%Ru CNU_3-$MgCO_3$ sample to follow on the changes of NH_3 and related N containing species during ammonia decomposition. As seen in Figure 6C and a peak at 667 cm^{-1} attributable to stretching of Ru-N with pyridine/pyrrole of support

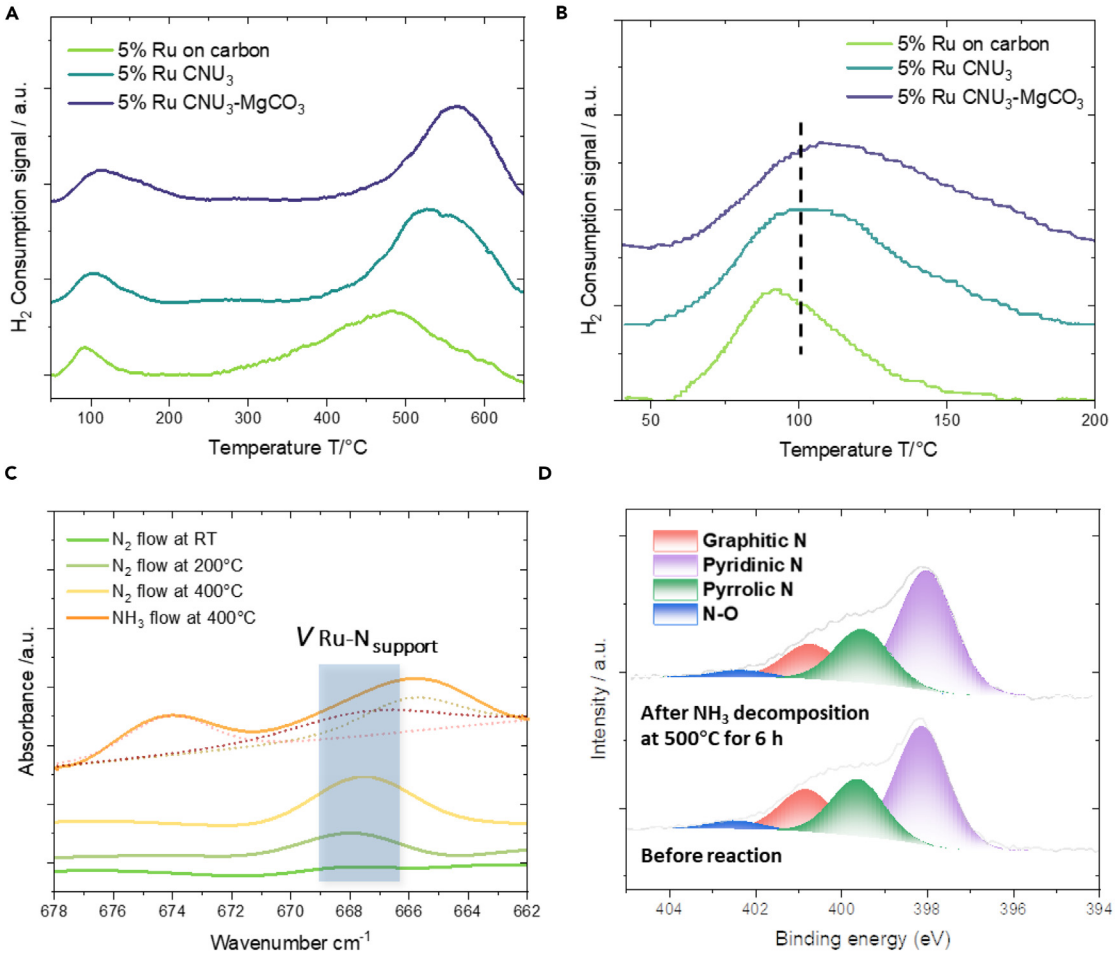

Figure 6. Further *in situ* and *ex situ* characterizations

(A) H_2-TPR of analogue samples.

(B) Enlarged figure of the H_2-TPR for the analogue samples focusing on the Ru metal reduction peak.

(C) *In-situ* FTIR of 5%Ru CNU_3-$MgCO_3$ support under different gas flow conditions and temperature at wavelength between 662 and 678 cm^{-1}.

(D) XPS of 5%Ru CNU_3-$MgCO_3$ sample before and after 6 h of ammonia decomposition at 500°C.

becomes visible under nitrogen flow(moisture from the porous material appears to block up such absorption peak).[42] Since no ammonia is yet purged through the IR chamber, the peak is thus accounted to the interaction between Ru and edge site nitrogen species from the support. This is also in agreement with the reported Ru-N asymmetric stretching peak of Ru (II) bipyridine complex,[43,44] which further confirms the Ru is anchored by the support sites with 4 N as stable surface coordination Ru complex. As the temperature gradually increases, the peak did not attenuate as seen by Figure 6C, which suggest their good thermal stability. Moreover, the at 667 cm^{-1} did not appear on the IR spectrum for 5%Ru on carbon material. This further implies the origin of the peak is coming from the interaction between Ru metal and the N on the support (Figure S9). The next question is that whether the N sites incorporated in carbon is involved as redox N in the ammonia decomposition. As ammonia is passed over the catalyst, two additional broad peaks arisen at 665 cm^{-1} and 675 cm^{-1}. The broad peak at 665 cm^{-1} can embrace the 667 cm^{-1} peak (no apparent attenuation in the deconvoluted peak) but a broadening peak at lower wavenumber can be attributed to the weaker Ru-NH_2 interaction.[45,46] This weaker stretching of Ru-N is unique when NH_3 is present in the gas phase. In addition, there is a simultaneous detection of stronger Ru-N at 675 cm^{-1} in NH_3 which matches with the formation of Ru=NH during the ammonia decomposition reaction. Similar blue shift in IR spectroscopy has been reported for other M = N-R and M-N-R_2 which support the assignment of peaks.[47] Thus, this suggests the direct identification of surface Ru-NH_x intermediates. It is not evident for the direct involvement of the structural N in the N-doped carbon since there is no apparent consumption of 667 cm^{-1} peak during the catalysis. Such structural N is highly conjugated with the 6 member-ring of pyridine or 5 member-ring in pyrrole in graphitic network so they are unlikely to cleave as redox sites under the reaction conditions. On the other hand, for a dissociative ammonia decomposition mechanism on Ru NPs, the N-H bonds are very labile and can be quickly broken to the kinetic more stable Ru≡N before their rate determining recombination to dinitrogen and complete the catalytic cycle. However, our *in situ* IR was unable to detect any absorption at around 880 cm^{-1} (Figure S10).[48] This could be due to the limited

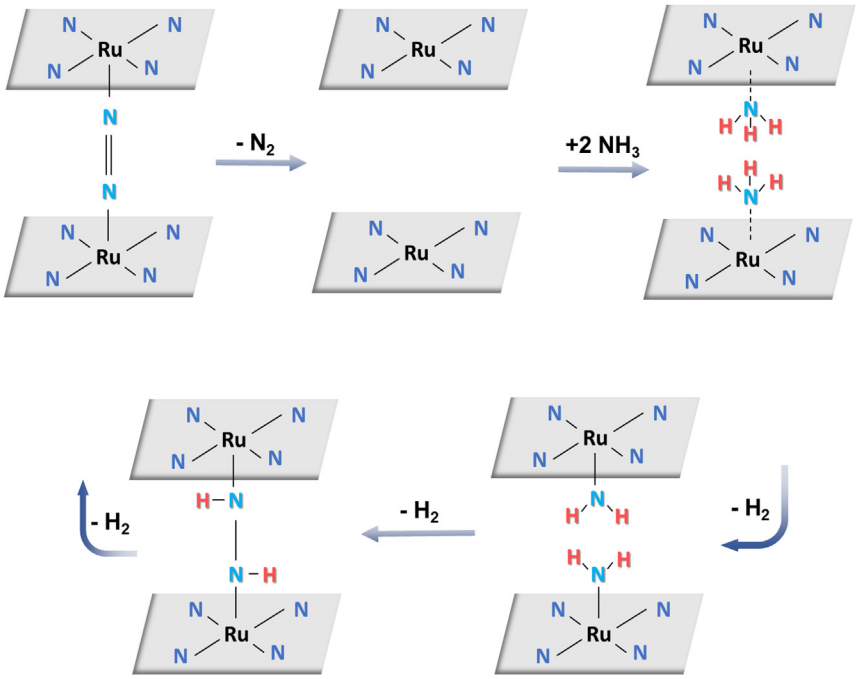

Figure 7. A schematic illustration of proposed associative mechanism with cleavage of single bonded Ru-N to form N_2

sensitivity of our technique but this may also be related to more predominant $RuNH_x$ intermediates rather than Ru≡N from the ammonia interaction indicative of the associative pathway. Thus, our FTIR characterization is consistent to the associative mechanism.

Besides, XPS characterization of 5%Ru CNU_3-$MgCO_3$ before reaction, after 6 h of NH_3 decomposition at 500°C and 400°C have also been carried out (Figure 6D and Table S5). No negligible changes were found for the distribution of different nitrogen species on the sample support before and after the ammonia decomposition reaction. This clearly suggest the structural nitrogen species as pyridinic or pyrrolic nitrogen does not involve in the ammonia decomposition in redox manner, which only offers the edge sites to stabilize Ru in 4 coordinated nitrogen configurations. The associative mechanism must be involved coupling of the two weakly adsorbed Ru-NH_2 species to form N_2.

Based on the above characterization, an associative mechanism for ammonia decomposition has been proposed for 5%Ru CNU_3-$MgCO_3$, as shown in Figure 7. Ammonia molecules are first physically adsorbed on to chelated Ru species. At elevated temperature, Ru will dissociate as the adsorbed NH_x to form chemically bonded Ru-NH_x intermediate species. The presence of the species is now confirmed by the Ru-N vibration peaks in the *in situ* FTIR. On this nitrogen doped carbon porous support, two adjacent Ru-NH_2 within the less rigid graphitic sheets in the mesopores could thus interact via a Ru-N(H)-N(H)-Ru in a stepwise manner. Further dissociation of N-H bonds would result in a Ru-N=N-Ru configuration without breaking the more energetic Ru≡N stepwise to dinitrogen and complete the catalytic cycle. The low apparent activation energy measured supports this reaction pathway.

Conclusion

In this work, we have successfully synthesized a nitrogen doped carbon material with high content of accessible N containing edge sites (pyridinic and pyrrolic) through a simple $MgCO_3$ template control combustion approach. The morphology and structure of the samples were analyzed by various characterization techniques, where induced meso- and macro-pores can be observed by SEM and BET as a result of CO_2 production during the calcination step. Compared to 5%Ru CNU_3, the $MgCO_3$ treated sample, 5%Ru CNU_3-$MgCO_3$ showed a significant rise in ammonia decomposition conversion from ca. 60% to ca. 90%. This was accompanied by a dramatic decrease in the activation energy from 81 to 43 kJ/mol.

In short summary, this study suggests associative mechanism is taken place over the 5%Ru CNU_3-$MgCO_3$ during ammonia decomposition but characterization discounts the direct involvement of nitrogen sites rather than coupling of two weakly RuN_x in close proximity in this mesoporous carbon. It is believed that the results can provide new inspirations on the fundamental understanding for future catalyst design.

Limitations of the study

Our work has demonstrated an excellent nitrogen doped carbon catalyst with abundant edge site nitrogen for highly efficient ammonia decomposition. The outstanding catalytic activity has been accounted to the distinct Ru ion anchored by 4 nitrogen site which facilitates associative ammonia decomposition. However, more direct evidence can help to solidify the proposed mechanism. Hence, we will make a further exploration by ^{15}N labeling experiments and theoretical calculations.

STAR★METHODS

Detailed methods are provided in the online version of this paper and include the following:

- KEY RESOURCES TABLE
- RESOURCE AVAILABILITY
  - Lead contact
  - Materials availability
  - Data and code availability
- EXPERIMENTAL MODEL AND SUBJECT DETAILS
- METHOD DETAILS
  - Synthesis of CNU_x
  - Synthesis of CNU_3-$MgCO_3$
  - Ru impregnation
  - Promoter metal impregnation
  - Ammonia decomposition catalysis
  - Material characterisation

SUPPLEMENTAL INFORMATION

Supplemental information can be found online at https://doi.org/10.1016/j.isci.2024.110571.

ACKNOWLEDGMENTS

We acknowledge financial support from the EPSRC Divisional CASE Conversion Incentivisation Scheme and OXGRIN, plc. The X-ray photoelectron (XPS) data collection was performed at the EPSRC National Facility for XPS ("HarwellXPS"), operated by Cardiff University and UCL, under Contract No. PR16195.

AUTHOR CONTRIBUTIONS

S.C.E.T. conceived and designed the research and analysis, reviewed and edited this manuscript. D.Y. carried out the catalyst preparation, thermocatalysis measurements, characterizations, and wrote the draft of manuscript. K.C.L. carried out the FTIR experiments. W.N. helped with the XAS analysis. M.D. performed the BET and SEM measurements. (S)TEM and EDS were collected and analyzed by P.L.H., ICP-MS results were calculated by D.S., XAS spectrum were taken by T.W. and Y.S. J.L. and S.W. gave technical support and helpful advice.

DECLARATION OF INTERESTS

The authors declare no competing interests.

Received: February 26, 2024
Revised: May 8, 2024
Accepted: July 20, 2024
Published: July 22, 2024

REFERENCES

1. Ye, D., and Tsang, S.C.E. (2023). Prospects and challenges of green ammonia synthesis. Nat. Synth. *2*, 612–623.
2. Bell, T.E., and Torrente-Murciano, L. (2016). H_2 Production via Ammonia Decomposition Using Non-Noble Metal Catalysts: A Review. Top. Catal. *59*, 1438–1457.
3. Mortensen, J.J., Hansen, L.B., Hammer, B., and Nørskov, J.K. (1999). Nitrogen Adsorption and Dissociation on Fe(111). J. Catal. *182*, 479.
4. García-García, F.R., Guerrero-Ruiz, A., Rodríguez-Ramos, I., Goguet, A., Shekhtman, S.O., and Hardacre, C. (2011). TAP studies of ammonia decomposition over Ru and Ir catalysts. Phys. Chem. Chem. Phys. *13*, 12892–12899.
5. Medford, A.J., Vojvodic, A., Hummelshøj, J.S., Voss, J., Abild-Pedersen, F., Studt, F., Bligaard, T., Nilsson, A., and Nørskov, J.K. (2015). From the Sabatier principle to a predictive theory of transition-metal heterogeneous catalysis. J. Catal. *328*, 36–42.
6. Zeinalipour-Yazdi, C.D., Hargreaves, J.S.J., Laassiri, S., Catlow, C.R.A., and Laassiri, S. (2021). A comparative analysis of the mechanisms of ammonia synthesis on various catalysts using density functional theory. R. Soc. Open Sci. *8*, 210952.
7. Chen, Y., Li, Z., Zhu, Y., Sun, D., Liu, X., Xu, L., and Tang, Y. (2019). Atomic Fe Dispersed on N-Doped Carbon Hollow Nanospheres for High-Efficiency Electrocatalytic Oxygen Reduction. Adv. Mater. *31*, 1–8.
8. He, L., Weniger, F., Neumann, H., and Beller, M. (2016). Synthesis, Characterization, and Application of Metal Nanoparticles Supported on Nitrogen-Doped Carbon: Catalysis beyond Electrochemistry. Angew. Chem., Int. Ed. Engl. *55*, 12582–12594.
9. Primo, A., Atienzar, P., Sanchez, E., Delgado, J.M., and García, H. (2012). From biomass wastes to large-area, high-quality, N-doped graphene: catalyst-free carbonization of chitosan coatings on arbitrary substrates. Chem. Commun. *48*, 9254–9256.
10. Khan, A., Goepel, M., Colmenares, J.C., and Gläser, R. (2020). Chitosan-Based N-Doped Carbon Materials for Electrocatalytic and Photocatalytic Applications. ACS Sustain. Chem. Eng. *8*, 4708–4727.
11. Luo, E., Xiao, M., Ge, J., Liu, C., and Xing, W. (2017). Selectively doping pyridinic and pyrrolic nitrogen into a 3D porous carbon matrix through template-induced edge engineering: enhanced catalytic activity towards the oxygen reduction reaction. J. Mater. Chem. A *5*, 21709–21714.
12. Chen, X., Oh, W.D., Zhang, P.H., Webster, R.D., and Lim, T.T. (2020). Surface

construction of nitrogen-doped chitosan-derived carbon nanosheets with hierarchically porous structure for enhanced sulfacetamide degradation via peroxymonosulfate activation: Maneuverable porosity and active sites. Chem. Eng. J. *382*, 122908.
13. Misra, A., Tyagi, P.K., Singh, M.K., and Misra, D.S. (2006). FTIR studies of nitrogen doped carbon nanotubes. Diam. Relat. Mater. *15*, 385–388.
14. Zhao, Q., Sun, J., Li, S., Huang, C., Yao, W., Chen, W., Zeng, T., Wu, Q., and Xu, Q. (2018). Single Nickel Atoms Anchored on Nitrogen-Doped Graphene as a Highly Active Cocatalyst for Photocatalytic H_2 Evolution. ACS Catal. *8*, 11863–11874.
15. Fang, H., Wu, S., Ayvali, T., Zheng, J., Fellowes, J., Ho, P.L., Leung, K.C., Large, A., Held, G., Kato, R., et al. (2023). Dispersed surface Ru ensembles on MgO(111) for catalytic ammonia decomposition. Nat. Commun. *14*, 647.
16. Peng, W., Liu, J., Liu, X., Wang, L., Yin, L., Tan, H., Hou, F., and Liang, J. (2023). Facilitating two-electron oxygen reduction with pyrrolic nitrogen sites for electrochemical hydrogen peroxide production. Nat. Commun. *14*, 4430.
17. Ayiania, M., Smith, M., Hensley, A.J., Scudiero, L., McEwen, J.S., and Garcia-Perez, M. (2020). Deconvoluting the XPS spectra for nitrogen-doped chars: An analysis from first principles. Carbon N. Y. *162*, 528–544.
18. He, S., Chen, G., Xiao, H., Shi, G., Ruan, C., Ma, Y., Dai, H., Yuan, B., Chen, X., and Yang, X. (2021). Facile preparation of N-doped activated carbon produced from rice husk for CO_2 capture. J. Colloid Interface Sci. *582*, 90–101.
19. Zhao, C., Wang, W., Yu, Z., Zhang, H., Wang, A., and Yang, Y. (2010). Nano-$CaCO_3$ as template for preparation of disordered large mesoporous carbon with hierarchical porosities. J. Mater. Chem. *20*, 976–980.
20. García-García, F.R., Álvarez-Rodríguez, J., Rodríguez-Ramos, I., and Guerrero-Ruiz, A. (2010). The use of carbon nanotubes with and without nitrogen doping as support for ruthenium catalysts in the ammonia decomposition reaction. Carbon N. Y. *48*, 267–276.
21. Chen, J., Zhu, Z.H., Wang, S., Ma, Q., Rudolph, V., and Lu, G.Q. (2010). Effects of nitrogen doping on the structure of carbon nanotubes (CNTs) and activity of Ru/CNTs in ammonia decomposition. Chem. Eng. J. *156*, 404–410.
22. Liu, H., Wang, H., Shen, J., Sun, Y., and Liu, Z. (2008). Promotion effect of cerium and lanthanum oxides on Ni/SBA-15 catalyst for ammonia decomposition. Catal. Today *131*, 444–449.
23. Zhang, J., Xu, H., and Li, W. (2005). Kinetic study of NH_3 decomposition over Ni nanoparticles: The role of la promoter, structure sensitivity and compensation effect. Appl. Catal. Gen. *296*, 257–267.
24. Wu, S., Peng, Y.K., Chen, T.Y., Mo, J., Large, A., McPherson, I., Chou, H.L., Wilkinson, I., Venturini, F., Grinter, D., et al. (2020). Removal of Hydrogen Poisoning by Electrostatically Polar MgO Support for Low-Pressure NH_3 Synthesis at a High Rate over the Ru Catalyst. ACS Catal. *10*, 5614–5622.
25. Bamufleh, H.S., and Zaman, S.F. (2023). Ammonia Decomposition over Alkali Metal (Li, K, Cs)-Promoted Bulk Mo2N Catalyst. Processes *11*, 2287.
26. Wang, Q., Guo, J., and Chen, P. (2021). The impact of alkali and alkaline earth metals on green ammonia synthesis. Chem *7*, 3203–3220.
27. Guo, X.Y., Wang, J.H., Zhang, Q., Li, T.Z., Dong, H., Jia, C.J., Li, C., and Zhang, Y.W. (2024). Alkaline earth metal promoted hydrogen production from ammonia decomposition over Ni/La_2O_3 -based catalysts. Appl. Catal. B Environ. Energy *348*, 123844.
28. Hill, A.K., and Torrente-Murciano, L. (2015). Low temperature H_2 production from ammonia using ruthenium-based catalysts: Synergetic effect of promoter and support. Appl. Catal. B Environ. *172–173*, 129–135.
29. Yin, S.F., Xu, B.Q., Ng, C.F., and Au, C.T. (2004). Nano Ru/CNTs: A highly active and stable catalyst for the generation of COx-free hydrogen in ammonia decomposition. Appl. Catal. B Environ. *48*, 237–241.
30. Yin, S.F., Xu, B.Q., Wang, S.J., Ng, C.F., and Au, C.T. (2004). Magnesia-carbon nanotubes (MgO-CNTs) nanocomposite: Novel support of Ru catalyst for the generation of CO_x-free hydrogen from ammonia. Catal. Lett. *96*, 113–116.
31. Chen, C., Wu, K., Ren, H., Zhou, C., Luo, Y., Lin, L., Au, C., and Jiang, L. (2021). Ru-Based Catalysts for Ammonia Decomposition: A Mini-Review. Energy Fuels *35*, 11693–11706.
32. Yin, S.F., Xu, B., Zhu, W., Ng, C., Zhou, X., and Au, C. (2004). Carbon nanotubes-supported Ru catalyst for the generation of C_x-free hydrogen from ammonia. Catal. Today *93–95*, 27–38.
33. Ren, S., Huang, F., Zheng, J., Chen, S., and Zhang, H. (2017). Ruthenium supported on nitrogen-doped ordered mesoporous carbon as highly active catalyst for NH_3 decomposition to H_2. Int. J. Hydrogen Energy *42*, 5105–5113.
34. Bell, T.E., Zhan, G., Wu, K., Zeng, H.C., and Torrente-Murciano, L. (2017). Modification of Ammonia Decomposition Activity of Ruthenium Nanoparticles by N-Doping of CNT Supports. Top. Catal. *60*, 1251–1259.
35. Zhang, T., Ju, X., Liu, L., Liu, L., He, T., Xu, Y., Wang, H., and Chen, P. (2023). Steering ammonia decomposition over Ru nanoparticles on ZrO_2 by enhancing metal-support interaction. Catal. Sci. Technol. *13*, 5205–5213.
36. Kim, H.B., and Park, E.D. (2023). Ammonia decomposition over Ru catalysts supported on alumina with different crystalline phases. Catal. Today *411–412*, 113817.
37. Ju, X., Liu, L., Yu, P., Guo, J., Zhang, X., He, T., Wu, G., and Chen, P. (2017). Mesoporous Ru/MgO prepared by a deposition-precipitation method as highly active catalyst for producing CO_x-free hydrogen from ammonia decomposition. Appl. Catal. B Environ. *211*, 167–175.
38. Li, L., Wang, Y., Xu, Z.P., and Zhu, Z. (2013). Catalytic ammonia decomposition for CO-free hydrogen generation over Ru/Cr_2O_3 catalysts. Appl. Catal. Gen. *467*, 246–252.
39. Lu, X., and Roldan, A. (2024). Ammonia cracking on single-atom catalysts: A mechanistic and microkinetic study. Appl. Catal. Gen. *673*, 119589.
40. Man, B., Zhang, H., Zhang, J., Li, X., Xu, N., Dai, H., Zhu, M., and Dai, B. (2017). Oxidation modification of Ru-based catalyst for acetylene hydrochlorination. RSC Adv. *7*, 23742–23750.
41. Madadi, S., and Kaliaguine, S. (2021). Activated Carbon-Supported Ruthenium as a Catalyst for the Solvent- And Initiator-Free Aerobic Epoxidation of Limonene. ACS Sustain. Chem. Eng. *9*, 10557–10568.
42. Adeniyi, A.A., and Ajibade, P.A. (2016). Exploring the Ruthenium-Ligands Bond and Their Relative Properties at Different Computational Methods. J. Chem. *15*, 3672062.
43. Garza-Ortiz, A., Uma Maheswari, P., Siegler, M., Spek, A.L., and Reedijk, J. (2013). A new family of Ru(ii) complexes with a tridentate pyridine Schiff-base ligand and bidentate co-ligands: Synthesis, characterization, structure and in vitro cytotoxicity studies. New J. Chem. *37*, 3450–3460.
44. Munshi, M.U., Martens, J., Berden, G., and Oomens, J. (2020). Vibrational Spectra of the Ruthenium-Tris-Bipyridine Dication and Its Reduced Form in Vacuo. J. Phys. Chem. A *124*, 2449–2459.
45. Allen, A.D., and Senoff, C.V. (1967). Preparation and infrared spectra of some ammine complexes of ruthenium(II) and ruthenium(III). Can. J. Chem. *45*, 1337–1341.
46. Dołega, D., Mikuli, E., and Chruszcz-Lipska, K. (2012). Experimental (FT-IR and FT-RS) and theoretical (QC-DFT) studies of vibrational modes and molecular structure of new low-temperature phases of $[Ru(NH_3)^6](BF_4)^3$ and $[Ru(NH_3)^6](ClO_4)^3$. Spectrochim. Acta Part A Mol. Biomol. Spectrosc. *98*, 132–141.
47. Stüker, T., Hohmann, T., Beckers, H., and Riedel, S. (2020). Fluoro Nitrenoid Complexes $FN{=}MF_2$ (M=Co, Rh, Ir): Electronic Structure Dichotomy and Formation of Nitrido Fluorides $N{\equiv}MF_3$. Angew. Chem. *132*, 23374–23379.
48. Pap, J.S., DeBeer George, S., and Berry, J.F. (2008). Delocalized metal-metal and metal-ligand multiple bonding in a linear Ru-Ru≡N unit: Elongation of a traditionally short Ru≡N bond. Angew. Chem., Int. Ed. Engl. *47*, 10102–10105.

STAR★METHODS

KEY RESOURCES TABLE

REAGENT or RESOURCE	SOURCE	IDENTIFIER
Chemicals, peptides, and recombinant proteins		
Chitosan	Sigma-Aldrich	CAS No.: 9012-76-4
Urea (99.8%+)	Alfa Aesar	CAS No.: 57-13-6
Ruthenium (III) chloride hydrate	Fluorochem Ltd	CAS No.: 14898-67-0
Lanthanum nitrate hexahydrate	Alfa Aesar	CAS No.: 10277-43-7
Cesium nitrate	Alfa Aesar	CAS No.: 7789-18-6
Magnesium carbonate	Sigma-Aldrich	CAS No.: 23389-33-5
5 wt. % Ru on Carbon	Sigma-Aldrich	CAS No.: mixture
Cerium nitrate hexahydrate	Alfa Aesar	CAS No.: 10294-41-4
Potassium nitrate	Alfa Aesar	CAS No.: 7757-79-1
Lithium nitrate	Alfa Aesar	CAS No.: 7790-69-4
Hydrochloric acid	Fisher chemical	CAS No.: 7647-01-0
Acetic acid	Sigma-Aldrich	CAS No.: 64-19-7
Ammonia	BOC Limited, a Linde company	CAS No.: 7664-41-7
Software and algorithms		
OriginPro 2023	Origin Lab	https://www.originlab.com/
CasaXPS v2.3.20PR1.0	Casa XPS	http://www.casaxps.com/
Athena	Athena XAS	https://bruceravel.github.io/demeter/documents/Athena/index.html
Other		
GC	Agilent	Agilent 7890A GC
SEM	JOEL	JSM-6610LV
TEM	JOEL	JEM2100
BET	Micromeritics	TriStar II Plus
ICP-MS	Shimadzu	ICPMS-2030
XRD	Bruker	D8 ADVANCE ECO
XPS	Kratos Analytical Limited	Kratos Axis Ultra-DLD
H_2-TPR	Anton Paar	ChemBET PULSAR ™ TPR/TPD - Chemisorption Analyzer
In situ FTIR	Thermo Scientific™	Nicolet™ iS50 FTIR Spectrometer
XAS	Huber	Huber 5021 diffractomete

RESOURCE AVAILABILITY

Lead contact

Further information and requests should be directed to and will be fulfilled by the lead contact, edman.tsang@chem.ox.ac.uk (Shik Chi Edman Tsang).

Materials availability

This study did not generate new unique reagents.

Data and code availability

- All data reported in this paper will be shared by the lead contact upon request.
- This study does not generate any original code.
- Any additional information required to re-analysed the data reported in this paper is available from the lead contact upon request.

EXPERIMENTAL MODEL AND SUBJECT DETAILS

This work does not use any experimental models.

METHOD DETAILS

Synthesis of CNU_x

Nitrogen doped carbon support was synthesized using a sol-gel method. Typically, 1 g of chitosan was mixed with 0, 1:1, 1:3 and 1:5 ratios (0, 1, 3 and 5 g) of urea. The mixture was dissolved in 40 mL of 5% acetic acid and subsequently dried at 80°C overnight. The desired nitrogen doped carbon powder (denoted as CNU_x x = Chitosan to Urea ratio) was synthesized by calcinating the precursor at 900°C for 2 h at a heating rate of 3°C/min under N_2 atmosphere.

Synthesis of CNU_3-$MgCO_3$

Controlled nitrogen doped carbon support was prepared via a similar procedure. A mixture consisting of 1 g of chitosan, 1 g of $MgCO_3$ and 3 g of urea was dissolved in 40 mL of 5% acetic acid. The solution was dried at 80°C overnight and subsequently calcined at 900°C for 2 h at a heating rate of 3°C/min under N_2 atmosphere. The as-obtained carbon powder was immersed in 40 mL 0.5 M HCl for 20 h, followed by washing with DI water until the pH value reached neutral.

Ru impregnation

5 wt. % of Ru was wetness impregnated on the carbon support using a 0.1 M ruthenium chloride solution. The mixture was sonicated for 1 h at 40°C before drying at 80°C overnight, followed by reduction at 450°C for 6 h at a heating rate of 5°C/min under 5% hydrogen/nitrogen atmosphere.

Promoter metal impregnation

5 wt. % of various promoter was wetness impregnated on the carbon support using a 0.1 M metal nitrate solution (i.e., $La(NO_3)_3$, $Ce(NO_3)_3$, KNO_3, $LiNO_3$ and $CsNO_3$). The mixture was sonicated for 1 h at 40°C before drying at 80°C overnight, followed by reduction at 450°C for 6 h at a heating rate of 5°C/min under 5% hydrogen/nitrogen atmosphere.

Ammonia decomposition catalysis

For a standard ammonia decomposition catalysis process, 50 mg of catalyst was packed in a quartz tube (4 mm i.d.) which was held vertically in a stainless steel fixed-bed flow reactor. The reaction temperature was raised to a desired temperature accompanied by designated ammonia flow rate. The resultant gas products were analyzed by an Agilent 7890A gas chromatography (GC) equipped with an 80/100 Porapak Q column and two thermal conductivity detectors (TCD).

Material characterisation

The structure of the synthesized sample was characterized by powder X-ray diffraction (XRD) using a Brucker D8 advanced Eco X-ray diffractometer operated at 40 kV and 25 mA with Cuα1 radiation; The Brunauer-Emmett-Teller (BET) surface area was obtained from N_2 adsorption/desorption isotherms at −196°C and analyzed by a Micromeritics TriStar II Plus instrument. All sorption isotherms were obtained using ultrahigh purity nitrogen gas (99.999%) to calculate the surface area and pore volume of the desired sample. The tested sample (approximately 100 mg) was loaded into a sample cell and pre-treated under vacuum of 10−5 Torr at 200°C for 18 h; To gain mechanistic understanding of the reaction, FTIR and *in situ* FTIR experiments were carried out on a Nicolet iS50 FT-IR spectrometer equipped with an MCT/A detector. For *in situ* experiments, 70 mg of sample was mixed with 50 mg of KBr and placed in a reactor cell. The system was then activated under N_2 flow (10 mL/min) at 400°C for 2 h. After the reactor cell cooled down, spectrums were taken from room temperature to 400°C with an increment of 100°C under continuous N_2 flow (10 mL/min). Further measurements were carried out under the same temperature conditions but flowing with 10% NH_3 in helium (10 mL/min) instead of N_2. The results were obtained by collecting 64 scans with a resolution of 4 cm^{-1}; Actual metal loading was calculated via Inductively coupled plasma mass spectrometry (ICP-MS). 10 mg of sample was digested in 5 mL of HCl (37%). The solution was diluted 1000 times using 25 mL volumetric flask. The concentration of the diluted sample was analyzed via ICP-MS; Structural information on the sample surface were gained by X-ray photoelectron spectroscopy (XPS) which was performed at the EPSRC National Facility for XPS ("HarwellXPS"). All the catalysts were pre-reduced in 5 wt % H2/N2 at 450°C for 6 h. The data was analyzed using CasaXPS v2.3.20PR1.0 software and peaks were fit with a Shirley background prior further analysis; The X-ray adsorption spectroscopy (XAS) data were collected at Beamline BL07A the Taiwan Light Source at National Synchrotron Radiation Research Center, Taiwan. The photon energy of the analogue sample was monitored using a Si (111) double crystal monochromator; Temperature-programmed reduction (TPR) experiments were performed in an automated flow chemisorption analyser (ChemBET Pulsar) to interpretate metal support interaction. 70 mg of sample was loaded in a U-shaped quartz tube, where the two ends were connected to a Swagelok fitting to allow the reactant gases to pass through the catalyst bed. The product stream was monitored continuously using a thermal conductivity detector (TCD). The sample was first pre-treated at 300°C for 1 h under pure He gas to remove any impurity or water from the surface. It was then cooled down to 40°C for 2 h so that a stable TCD baseline was obtained. Subsequently, the reactor was heated up to 700°C at a ramp rate of 5°C/min under 5% H_2/N_2 flow (20 mL/min) and the H_2 consumption is analyzed.